Flux enhancement of radiation belt electrons during geomagnetic storms driven by coronal mass ejections and corotating interaction regions

Ryuho Kataoka[1,2,3] and Yoshizumi Miyoshi[1]

Received 21 November 2005; revised 20 April 2006; accepted 20 April 2006; published 20 September 2006.

[1] A meteorological view of solar wind structures is useful for probability prediction of the flux enhancement of radiation belt electrons. We report the averaged variations of the solar wind parameters and radiation belt electrons during isolated geomagnetic storms driven by coronal mass ejections (CMEs) and corotating interaction regions (CIRs), using a superposed epoch analysis centered on interplanetary shocks and stream interfaces, respectively, whose arrival times can be used as a precursor for the flux enhancement. A total of 49 CME- and 6 CIR-associated storms with $Dst < -100$ nT are identified during solar cycle 23 from January 1996 to December 2004. In CME-associated storms, the average flux recovers to the prestorm level about 2 days after a shock arrival. The occurrence probability of the >2 MeV electron flux alert with $>10^3$ pfu (pfu = particles cm^{-2} s^{-1} sr^{-1}) at geosynchronous orbit 1 day after the shock is only 14% (7 of 49 events) and is smaller than the prestorm level, while the probability 4 days after the shock increases to 43% (21 of 49 events) and is larger than the prestorm level. In CIR-associated storms, the average flux recovers to the prestorm level about 1 day after a stream interface arrival. The probability of an electron flux alert is 83% (5 of 6 events) 1 day after the stream interface arrival and remains at that level for at least the next 4 days.

Citation: Kataoka, R., and Y. Miyoshi (2006), Flux enhancement of radiation belt electrons during geomagnetic storms driven by coronal mass ejections and corotating interaction regions, *Space Weather*, *4*, S09004, doi:10.1029/2005SW000211.

1. Introduction

[2] Modern life depends on satellite observations and communications. Thus large enhancements of the radiation belt electron flux can sometimes cause a serious problem, because these energetic particles can cause deep dielectric charging of satellites, which in turn can lead to spacecraft anomalies and/or complete failure [*Baker et al.*, 1987, 1998]. The radiation belt environment drastically changes particularly during geomagnetic storms. It is generally well known that the electron flux decreases during the main phase and then recovers and often increases at the end of the main phase and during the recovery phase [*Friedel et al.*, 2002; *Miyoshi et al.*, 2003]. The strength of the flux enhancement during the recovery phase is not well correlated with the minimum *Dst* index, and only about a half of moderate or intense storms with $Dst < -50$ nT result in the flux enhancement exceeding the prestorm level [*Reeves et al.*, 2003].

[3] The variability of the electron flux is largely controlled by the solar wind. There is a good correlation between the flux enhancement and the solar wind speed [e.g., *Paulikas and Blake*, 1979; *Baker et al.*, 1986]. At NOAA/SEC, the Relativistic Electron Forecast Model (REFM, http://www.sel.noaa.gov/refm) uses a linear prediction filter [*Baker et al.*, 1990] with the solar wind speed as its input to predict the >2.0 MeV electron flux at geosynchronous orbit. The southward component of the interplanetary magnetic field (IMF) is also known to be another important parameter that promotes flux enhancements [*Blake et al.*, 1997; *Li et al.*, 2005]. Using the radial diffusion equation [*Li et al.*, 2001; *Li*, 2004; *Barker et al.*, 2005] with these two solar wind parameters as inputs, University of Colorado provides forecasts of the daily variation in the electron flux (http://lasp.colorado.edu/space_weather/xlf3/xlf3.html).

[4] New ways to understand this solar wind parameter dependence are emerging from the fact that most storms are associated with the large-scale solar wind structures,

[1]Solar-Terrestrial Environment Laboratory, Nagoya University, Nagoya, Japan.
[2]National Institute of Information and Communications Technology, Tokyo, Japan.
[3]NASA Goddard Space Flight Center, Greenbelt, Maryland, USA.

such as coronal mass ejections (CMEs) and corotating interaction regions (CIRs) [*Gonzalez et al.*, 1999], where the solar wind parameters change depending on the solar wind structures. It has been reported that the CIR-driven storms are more effective for the flux enhancement at geosynchronous orbit than are CME-driven storms [*Dmitriev et al.*, 2005; *Miyoshi and Kataoka*, 2005], while the CME-driven great storms are more effective for the flux enhancement at the inner portion at $L < 3$ [*Miyoshi and Kataoka*, 2005]. Using a superposed epoch analysis centered on the *Dst* minima of CIR- and CME-driven storms, *Miyoshi and Kataoka* [2005] showed that the flux enhancement at geosynchronous orbit is not only dependent on the solar wind speed but also on the Alfvénic fluctuations of the IMF, which are embedded within the coronal hole stream following a CIR.

[5] The first motivation of this study is to predict the radiation belt response to the solar wind structures that can produce severe storms. In order to minimize the ambiguity of the storm event selections and identifications of the solar wind driver, this paper focuses on only isolated intense storms with $Dst < -100$ nT during solar cycle 23 as identified by *Miyoshi and Kataoka* [2005]. Although CMEs cause most intense storms and CIRs tend to cause only weak or moderate storms [*Tsurutani et al.*, 1995], it is now possible to compare the intense storms driven by CMEs and CIRs directly because we have comprehensive data sets of a number of CME-associated storms and several rare CIR-associated intense storms during solar cycle 23.

[6] Extending from the analogy of the meteorological air mass concept [*McPherron and Siscoe*, 2004], CMEs and CIRs can be regarded as the counterpart of the hurricane and cold front, respectively. Furthermore, analogous to the probability of precipitation in weather forecasting, the occurrence probabilities of killer electrons exceeding an alert level should be meaningful for the space weather forecasting. In this paper, we quantify the occurrence probability of "killer electrons" associated with CMEs and CIRs for the first time. Interplanetary shocks and stream interfaces are the most distinct discontinuities associated with CMEs and CIRs, respectively, whose arrival times may be used as a precursor for the flux enhancement. Applying a superposed epoch analysis about the shocks and stream interfaces accompanied by isolated intense storms during solar cycle 23, we report the averaged variations of the solar wind parameters and radiation belt electrons, and the occurrence probability of the electron flux alert after the shock/stream interface arrivals.

2. Event Selection

[7] Figure 1 schematically illustrates the typical structure of CMEs and CIRs. Interplanetary shocks can be identified before CME arrivals as sudden increases in the IMF strength, solar wind speed, densities, and temperatures. A sheath region of compressed, hot, and turbulent

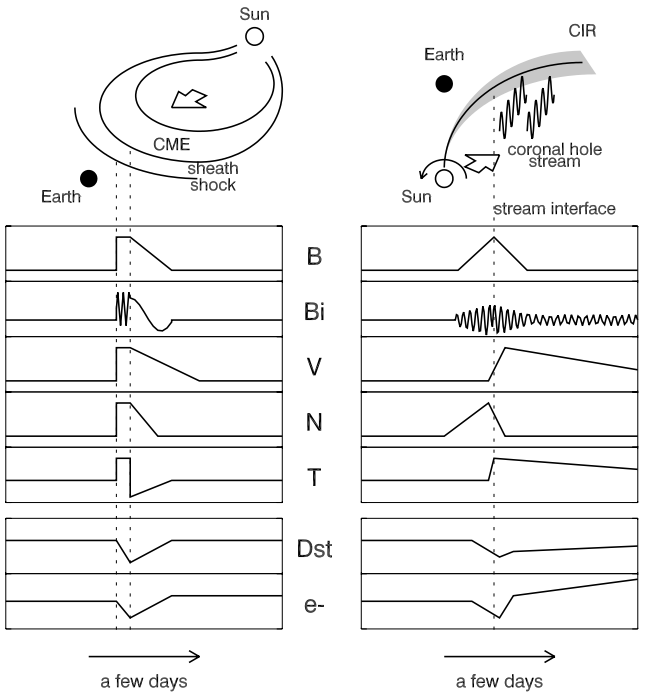

Figure 1. Schematic illustration of typical solar wind structures of coronal mass ejections (CMEs) and corotating interaction regions (CIRs): (top to bottom) magnetic field strength B, one of the Cartesian component B_i, solar wind speed V, density N, temperature T, expected response of the *Dst* index, and >2.0 MeV electron flux at geosynchronous orbit.

plasma containing many discontinuities exists downstream of the shock [*Kataoka et al.*, 2005a], and extremely cold plasma occasionally with a strong and smoothly rotating IMF follows the sheath region [e.g., *Burlaga et al.*, 2001]. The cold plasma region could be identified with the "CME" indicated in Figure 1. In CIRs, stream interfaces correspond to an increase in the solar wind speed and temperature and a decrease in the density [e.g., *Burlaga*, 1974; *Gosling et al.*, 1978]. A useful signature marking the stream interface is a directional change in the azimuthal flow angle from westward (in the direction of solar rotation) to eastward. A slow stream occasionally associated with a heliospheric current sheet [*Smith*, 2001] is compressed ahead of the stream interface, while a high-speed stream with large-amplitude Alfvénic fluctuations originating from a solar coronal hole follows the stream interface [*Tsurutani et al.*, 2006]. A gradual density increase with the westward flow deflection exists about a half day before the arrival of the stream interface [*McPherron et al.*, 2005]. It is worthwhile noting here that, as shown in this picture, a CME-related disturbance is nearly a radial profile of the solar wind structure, while a CIR-related disturbance is nearly an azimuthal profile. The temporal-

Table 1. Event List of CME-Associated Storms With *Dst* < −100 nT From January 1996 to December 2004[a]

Event	Arrival Date[b]	UT, Hour	*dT*, Hour	*Dst*, nT
A01	1997/05/15	1	11	−115
A02	1997/10/10	15	12	−130
A03	1997/11/06	22	6	−110
A04	1997/11/22	9	21	−108
A05	1998/05/03	17	12	−205
A06	1998/06/25	16	12	−101
A07	1998/08/06	7	4	−138
A08	1998/08/26	6	27	−155
A09	1998/09/24	23	10	−207
A10	1998/10/18	19	20	−112
A11	1998/11/12	6	39	−131
A12	1999/01/13	10	13	−112
A13	1999/02/18	2	15	−123
A14	1999/09/22	11	12	−173
A15	1999/10/21	1	29	−237
A16	1999/11/13	12	10	−106
A17	2000/02/11	23	12	−133
A18	2000/04/06	16	8	−288
A19	2000/05/23	23	9	−147
A20	2000/07/15	13	11	−301
A21	2000/09/17	15	8	−201
A22	2000/10/05	2	11	−182
A23	2000/10/12	21	41	−107
A24	2000/10/28	6	21	−127
A25	2000/11/06	9	12	−159
A26	2000/11/28	4	33	−119
A27	2001/03/19	10	27	−149
A28	2001/03/31	0	8	−387
A29	2001/04/11	13	10	−271
A30	2001/04/18	0	6	−114
A31	2001/04/21	15	24	−102
A32	2001/08/17	10	11	−105
A33	2001/09/25	20	5	−102
A34	2001/10/21	16	5	−187
A35	2001/10/28	2	9	−157
A36	2001/11/06	1	5	−292
A37	2001/11/24	5	11	−221
A38	2002/03/23	11	22	−100
A39	2002/05/11	9	10	−110
A40	2002/05/23	10	7	−109
A41	2002/08/01	22	7	−102
A42	2002/08/20	13	7	−106
A43	2003/05/29	18	8	−131
A44	2003/06/18	4	5	−145
A45	2003/08/17	13	26	−168
A46	2003/11/20	7	12	−472
A47	2004/01/22	0	13	−149
A48	2004/04/03	9	15	−112
A49	2004/08/29	9	37	−126

[a]From left to right, shown are the event number, arrival time of the shocks, time separation between the shock and the minimum *Dst*, and the minimum *Dst* index.
[b]Dates are given in the format year/month/day.

spatial scales are therefore essentially different between CMEs and CIRs: A single CME-related disturbance basically last only a few days, while a high-speed stream from a large coronal hole sometimes can last up to a week. Extending the results from *Miyoshi and Kataoka* [2005], the expected responses of the ring current and radiation belt are summarized in the bottom two plots. Starting from this qualitative picture, we examine the averaged variation quantitatively via a superposed epoch analysis about shocks and stream interfaces.

[8] Using the OMNI-2 data for the time interval from January 1996 to December 2004, we identified a total of 49 isolated storms with *Dst* < −100 nT accompanied by shocks and 6 accompanied by stream interfaces. In this paper, ''CME-associated storms'' are defined by the existence of interplanetary shocks followed by extremely low temperatures less than a half of the empirically expected temperature [*Lopez*, 1987; *Richardson and Cane*, 1995], while ''CIR-associated storms'' are defined by the existence of a stream interface and a trailing high-speed coronal hole stream. Table 1 summarizes the CME-associated storms with UT hours just before the shock arrival. When multiple shocks are found within 24 hours, we selected the most significant shock with the largest velocity jump.

[9] Table 2 summarizes the CIR-associated storms with the UT hours just before the stream interface arrival. All of the events listed in Table 2 have been investigated in detail by *Richardson et al.* [2006]. Note also that the category of ''CIR storms'' of *Miyoshi and Kataoka* [2005] includes some CIR structures merged with CMEs, while we eliminated such merged CIRs from the category of the CIR-associated storms in this paper. The small number of CIR-associated storms is not unusual because CIR-associated storms are generally weak to moderate and the *Dst* index rarely reaches −100 nT [*Tsurutani et al.*, 1995]. In fact, the average value of *Dst* minima in CIR-associated storms in this study is only −113 nT. Conducting similar surveys including weaker CIR-associated storms with *Dst* > −100 nT may be therefore worthwhile in future work. Although intense CIR-associated storms are rare, the investigation of such events is quite important because the CIR-associated storms can be the severest events in terms of the flux enhancement. For example, according to a newspaper article published by *Nihon Keizai Shimbun* [2004], a broadcasting program by Japanese satellites was disrupted for about 45 min on 14 February 2004 during the extreme flux enhancement after the 12 February 2004 storm (B6).

[10] Table 3 shows 23 other storms with *Dst* < −100 nT, which were eliminated from this study because of multiple storm occurrences within 4 days (20 events), nonexistence of

Table 2. Event List of CIR-Associated Storms With *Dst* < −100 nT From January 1996 to December 2004[a]

Event	Arrival Date[b]	UT, Hour	*dT*, Hour	*Dst*, nT
B1	1996/10/22	19	9	−105
B2	1998/03/10	12	8	−116
B3	2002/10/14	13	0	−100
B4	2002/11/21	6	4	−128
B5	2003/07/11	19	10	−118
B6	2004/02/12	2	−9	−109

[a]From left to right, shown are the event number, arrival time of stream interface, time separation between the stream interface and the minimum *Dst*, and the minimum *Dst* index.
[b]Dates are given in the format year/month/day.

Table 3. Event List of Other Storms With *Dst* < −100 nT From January 1996 to December 2004

Event	Storm Date[a]	UT, Hour	*Dst*, nT	Notes[b]
C01	1997/04/21	23	−107	no shock
C02	1998/02/18	0	−100	no shock
C03	1998/11/08	6	−149	multi
C04	1998/11/09	17	−142	multi
C05	2000/08/11	6	−106	multi
C06	2000/08/12	9	−235	multi
C07	2001/10/01	8	−148	multi
C08	2001/10/03	14	−166	multi
C09	2002/04/18	7	−127	multi
C10	2002/04/20	8	−149	multi
C11	2002/09/04	5	−109	multi
C12	2002/09/08	0	−181	multi
C13	2002/10/01	16	−176	multi
C14	2002/10/04	8	−146	multi
C15	2002/10/07	7	−115	multi
C16	2003/07/16	12	−117	CHS
C17	2003/10/30	0	−363	multi
C18	2003/10/30	22	−401	multi
C19	2004/07/23	2	−101	multi
C20	2004/07/25	11	−148	multi
C21	2004/07/27	13	−197	multi
C22	2004/11/08	6	−373	multi
C23	2004/11/10	9	−289	multi

[a]Dates are given in the format year/month/day.
[b]Notes are multi, multiple occurrence of storms within 4 days; no shock, nonexistence of shocks; and CHS, the storms associated with coronal hole streams as explained in detail by *Richardson et al.* [2006].

shocks (C01, C02), or nonexistence of stream interfaces (C16). Referring to Tables 1 and 3, it is noteworthy here that the occurrence probability of shocks are quite high (49 of 51 events, 96%) for CME-driven isolated storms with *Dst* < −100 nT, consistent with the classical understanding of storms with a sudden commencement (Ssc-type storms) and gradual commencement (Sg-type storms) [e.g., *Yoshida et al.*, 2004].

[11] Let us summarize Tables 1, 2, and 3 by making histograms. The annual occurrences of CIR-(blue) and CME-associated (red) storms are shown in Figure 2a. As pointed out by *Richardson et al.* [2006], CIR-associated storms are not found around the solar maximum in 1999, 2000, and 2001. On the other hand, CME-associated storms are more frequent in the solar maximum than in the solar minimum. Multiple storm occurrences (orange) are frequently found in the declining phase. Figure 2b shows the histograms of the storm amplitude. CIR-associated storms never reach the level of *Dst* < −140 nT, while 22 of 49 CME-associated storms have *Dst* < −140 nT. The multiple storms, defined by more than one storms occurred within 4 days, tend to have large amplitudes with *Dst* < −140 nT (15 of 20 multiple storms) because these events are often associated with multiple halo CMEs during extreme solar activities. In fact, the multiple storms include the recent space weather events of October 2003 (C17, C18), July 2004 (C19, C20, C21), and November 2004 (C22, C23), as shown in Table 3. In this paper, we do not further discuss the multiple storms, and focus only on the isolated storms.

[12] Figure 2c shows the histograms of the delay between the shocks/stream interfaces and minimum *Dst*. The minimum *Dst* defines the beginning of the recovery phase, and therefore can be regarded as a proxy for the beginning of the flux enhancement of radiation belt

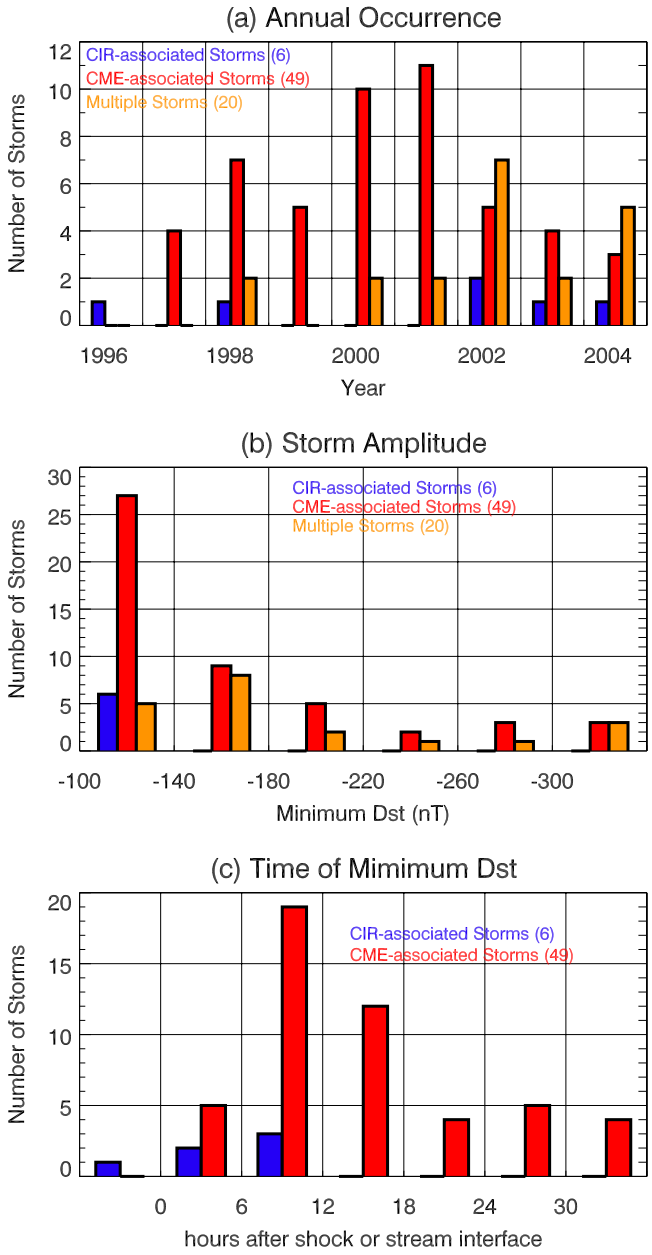

Figure 2. Histograms of (a) annual storm occurrence, (b) storm amplitude, and (c) time of minimum *Dst*. CME- and CIR-associated storms are shown in red and blue, respectively, and multiple storms are shown in orange. The minimum *Dst* times are measured from shocks (red) and stream interfaces (blue).

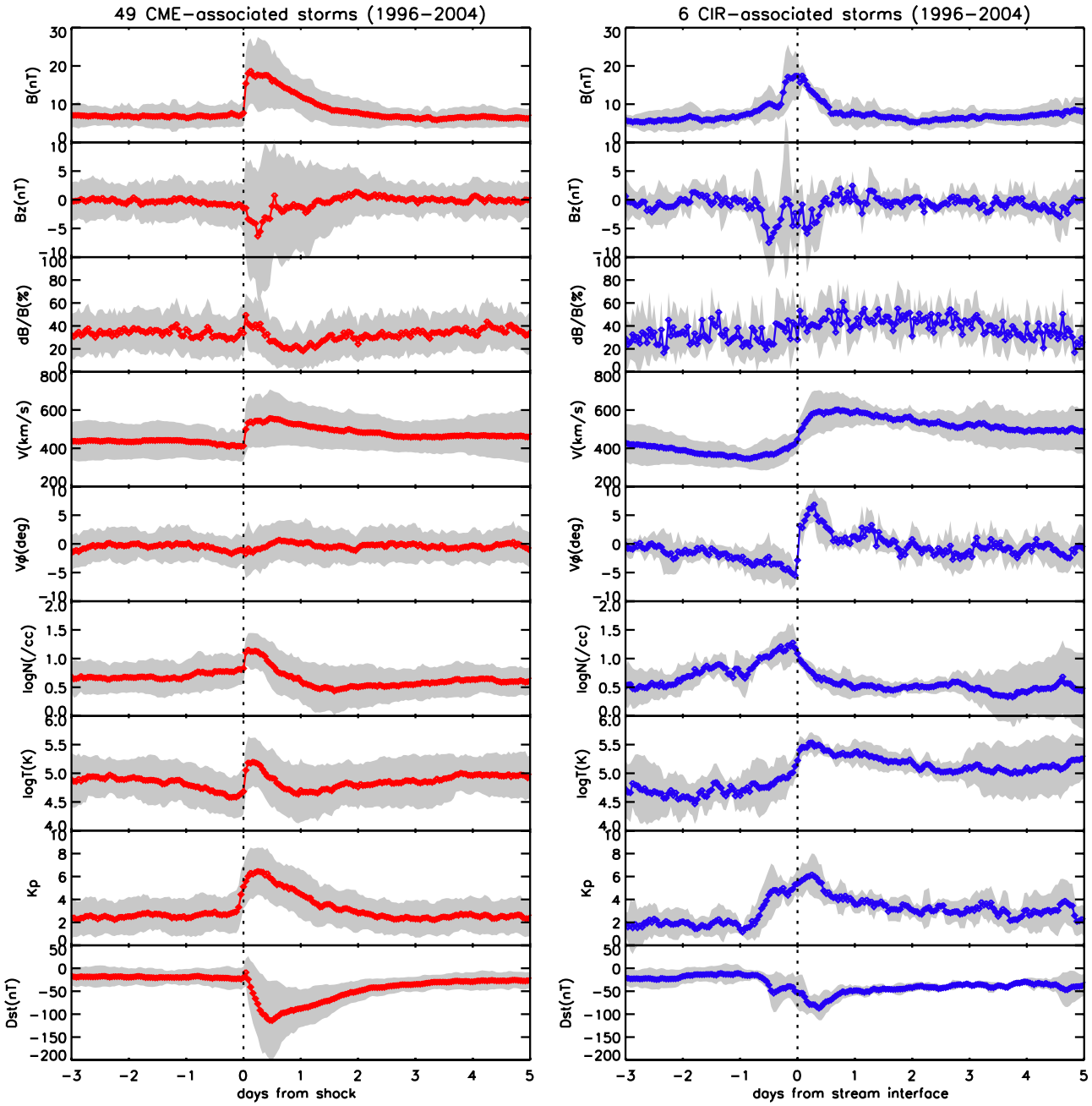

Figure 3. Averaged solar wind parameters superposed at (left) shocks and (right) stream interfaces during CME- and CIR-associated storms, respectively. Shown are (top to bottom) the magnetic field strength B, the B_z component, fluctuation level dB/B, solar wind speed V, azimuthal flow angle $V\phi$, proton number densities N, proton temperatures T, averaged Kp index, and averaged Dst index. The gray region indicates the standard deviation.

electrons. After a shock arrival, the most frequent delay is 6−12 hours (19 of 49 events). 25 events have a delay greater than 12 hours. This result provides the simplest probability prediction for the onset of the flux enhancement after the arrival of a shock. On the other hand, stream interfaces are not such a rigid precursor, and sometimes the minimum Dst can even precede the stream interface.

3. Solar Wind Structures

[13] Figure 3 shows the results of a superposed epoch analysis of the solar wind parameters using the OMNI-2

data set. The time resolution of the OMNI-2 data set is 1 hour. The reference time $t = 0$ is the arrival time of shocks and stream interfaces for CME- and CIR-associated storms, respectively. Densities and temperatures are averaged after taking the logarithm because the $\log_{10}$ values better follow the Gaussian distribution, and the mean values and standard deviations are more meaningful. As a proxy of the fluctuation level of magnetic fields, we use the standard deviation of magnetic field vectors dB normalized by the magnetic field strength B. In the OMNI-2 data set, dB is defined by $dB = (dB_x^2 + dB_y^2 + dB_z^2)^{0.5}$, where dB_i is the standard deviation of the B_i component during 1 hour. Gray regions show the standard deviations. The averaged solar wind parameters change depending on the inherent plasma properties of the solar wind structures as shown below.

[14] In the left plots of Figure 3, the average shock profile is identified at $t = 0.0$ days, where sudden changes in all of the parameters are observed except for the azimuthal flow angle. Sheath-like plasma follows the shock for the time interval from $t = 0.0$ to 0.5 days, where the magnetic field fluctuation levels, densities, and temperatures are particularly higher than average. The average main phase corresponds to the sheath-like plasma region. This result is consistent with the fact that the number of sheath-driven storms is significantly larger than that of magnetic cloud-driven storms [*Huttunen and Koskinen*, 2004]. The average recovery phase after $t = 0.5$ day corresponds to the ejecta-like plasma region where the magnetic field fluctuation level and temperatures are lower than average. The overall averaged disturbances of CMEs last about 3 days from $t = 0.0$ to 3.0 days, and the plasma parameters return to the prestorm levels after $t = 3.0$ days.

[15] In the right-hand plots of Figure 3, the average stream interface profile is identified at $t = 0.0$ days, where increases in the solar wind speed and temperatures are observed with a decrease in density. The sign of the azimuthal flow angle sharply changes from negative to positive, and the magnetic field strength reaches its maximum around the stream interface. There is an extremely quiet period of average $Kp \sim 1.0$ within a slow stream at $t = -1.0$ day before the stream interface [*Borovsky and Steinberg*, 2006], and this quiet period may have a potential as a precursor. After $t = -1.0$ day, a significant density enhancement begins with some negative deflection of azimuthal flow angles, and the magnetic field fluctuations start increasing. After the stream interface at $t = 0.0$ days, coronal hole streams with strong Alfvénic fluctuations are clearly found, where the solar wind speed, temperatures, and the magnetic field fluctuation level are higher than average with densities lower than average. The overall averaged disturbances of CIRs last more than 6 days, i.e., about twice that of single CME-associated disturbance.

[16] Figure 4 shows some derived solar wind and magnetospheric parameters. In this paper, we define the "fluctuating electric field" as the product of V and dB. This is a useful parameter to evaluate the maximum strength of the motional electric field associated with the Alfvénic fluctuations because the solar wind is usually Alfvénic [*Belcher and Davis*, 1971] and the standard deviations of the solar wind velocity are relatively small. It is worth noting here that the fluctuation level dB/B in Figure 3 can be interpreted as the strength of the fluctuating electric field normalized by the maximum strength of the interplanetary motional electric field. After $t = 0.5$ day, during the recovery phase, the fluctuating electric field is stronger in CIR-associated storms because of the high-speed and highly Alfvénic nature of the coronal hole stream. The plasma β, the ratio of the plasma thermal pressure to magnetic pressure, is extremely low during the recovery phase of CME-associated storms because of extremely low temperature plasma and strong magnetic fields, while the Alfvén Mach number Ma is significantly higher in CIR-associated storms because of both the high-speed flow and weaker magnetic field. During the recovery phase from $t = 0.5$ to 1.5, the averaged magnetosonic Mach number $M_{ms} \sim 4.0$ in CME-associated storms, while $M_{ms} \sim 6.0$ in CIR-associated storms. In this paper, magnetosonic speed is approximated as $(V_s^2 + V_A^2)^{0.5}$, where V_s is the sound speed and V_A is the Alfvén speed.

[17] The subsolar magnetopause distance MP is estimated from the empirical model by *Shue et al.* [1998], which depends on the dynamic pressure and B_z. The polar cap potential is estimated from the Hill model [*Siscoe et al.*, 2002]. We used the formulation by *Ober et al.* [2003], which depends on the solar wind speed, dynamic pressure, B_y, B_z, and $F_{10.7}$. In CME-associated storms, the averaged magnetopause distance gradually recovers to the prestorm level after the sheath compression, while in CIR-associated storms the averaged magnetopause distance rapidly recovers to the prestorm level because of the sudden density drop after the stream interface. The averaged polar cap potential shows similar trend that the potential drop gradually decreases in CME-associated storms and rapidly decreases in CIR-associated storms. These variations of magnetopause and polar cap potential are closely related to the broad distribution of southward B_z in 2 days after the arrival of a shock and the narrow distribution of southward B_z in 0.5 day after the arrival of a stream interface.

4. Radiation Belt Response

[18] In situ measurements of the >2.0 MeV electrons at geosynchronous orbit are available from the GOES satellites. We use the data from GOES 8 and 10, before and after July 2003, respectively. Figure 5 shows the result of the superposed epoch analysis for >2.0 MeV electron flux observed by the GOES satellites. In this study, we eliminated time periods when the energetic protons may contaminate the electron detector. We average the flux after taking the logarithm because the $\log_{10}$ flux follows the Gaussian distribution more closely, and the mean values

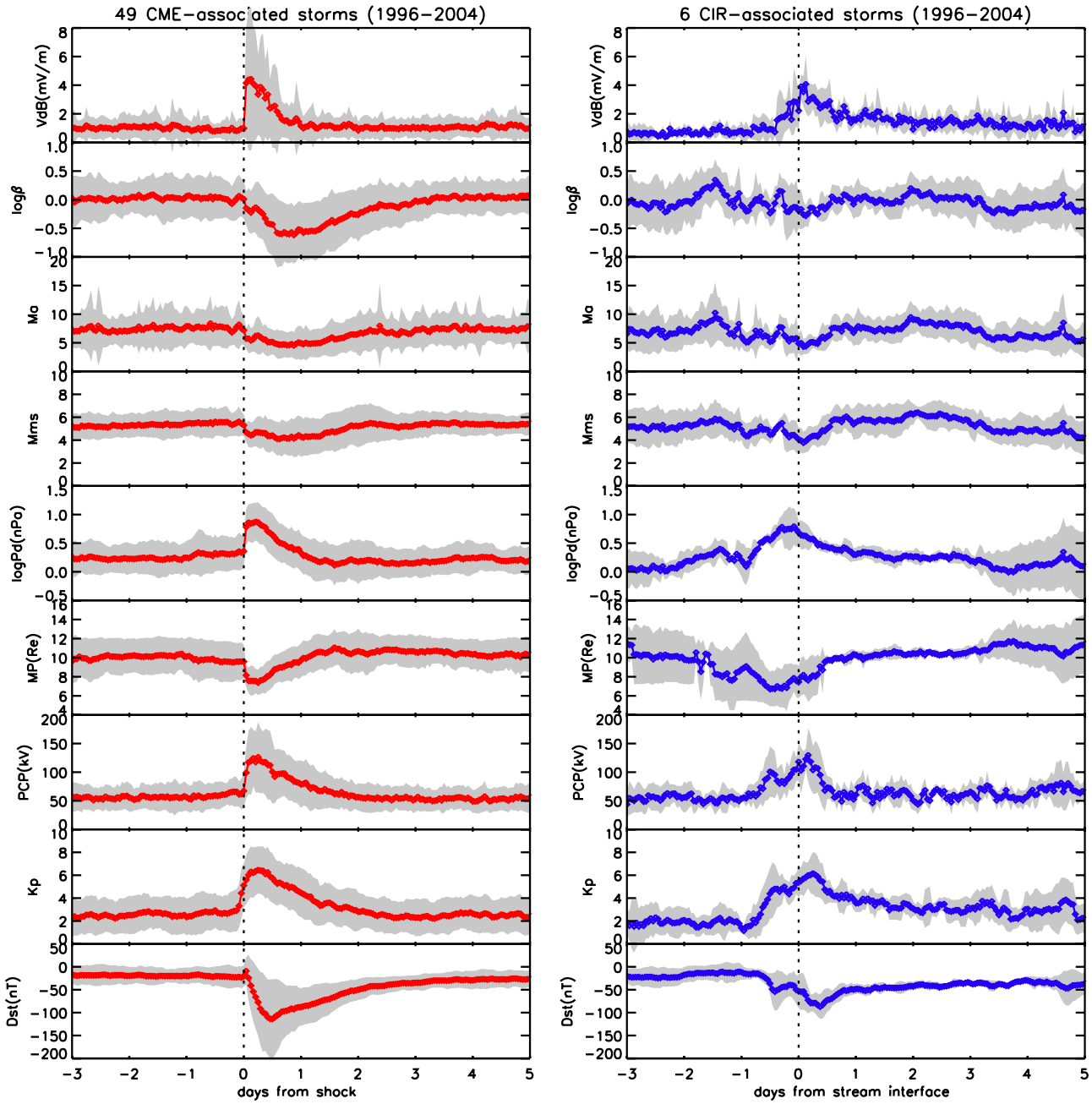

Figure 4. Derived solar wind parameters superposed at (left) shocks and (right) stream interfaces during CME- and CIR-associated storms, respectively. Shown are (top to bottom) the fluctuating electric fields V_{dB}, plasma β, Alfvén Mach number *Ma*, magnetosonic Mach number M_{ms}, dynamic pressure *Pd*, subsolar magnetopause distance *MP*, polar cap potential *PCP*, averaged *Kp* index, and averaged *Dst* index. The gray region indicates the standard deviation.

and standard deviations are more meaningful. The most prominent flux variation at geosynchronous orbit is the decrease which occurs in the main phase followed by the increase in the recovery phase. In CME-associated storms, such a variation is clearly seen even though they are superposed about the interplanetary shocks. On the other hand, in CIR-associated storms, large flux decreases are found before and after the stream interface because the storm main phase sometimes exists before and after the stream interface [see *Richardson et al.*, 2006]. The diurnal variation is smoothed out in the averaged values of CME-associated storms, while a significant diurnal variation

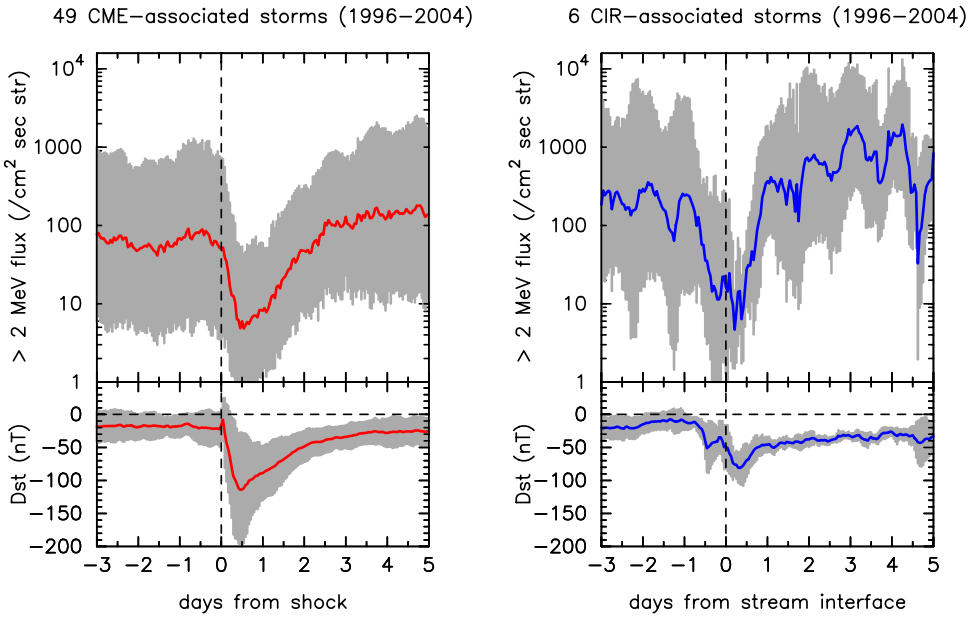

Figure 5. Averaged $\log_{10}$ flux of >2.0 MeV electrons measured by the GOES satellites superposed about shocks and stream interfaces during (left) CME- and (right) CIR-associated storms, respectively. Averaged *Dst* is also shown in the bottom plots. The gray region indicates the standard deviation.

remains in the CIR-associated storms because of the small number of events. The recovery of the averaged flux is faster and stronger in CIR-storms. A two-step evolution of the flux enhancement may be found in the recovery trends of the averaged flux in both cases. In CME-associated storms, the averaged flux recovers to the prestorm level from t = 0.5 to 2.5 days, and there is only a small evolution in the averaged flux after t = 2.5 days. On the other hand, in CIR-associated storms, the averaged flux rapidly recovers to the prestorm level from t = 0.5 to 1.5 days, and gradually enhances to the 10^3 pfu (pfu = particles cm^{-2} s^{-1} sr^{-1}) level from t = 1.5 to 3.5 days.

[19] Radiation belt electrons can be monitored over a wide range of L value by the low-altitude NOAA/POES satellites. We used NOAA 12 and 15 satellites, orbiting 0730−1930 local time, which produce the data before and after 1 July 1998, respectively. We used the 90° and >300 keV electron detectors which mostly measure local mirroring electrons [*Evans and Greer*, 2000]. Figure 6 shows the superposed $L - t$ diagrams of radiation belt electrons for CME- and CIR-associated storms, respectively. Again, we average the flux after taking the logarithm. Note that the L value in this study is McIlwain's L derived from IGRF (see *Miyoshi et al.* [2003] for details of our NOAA data analysis). Since the >300 keV electron detector is also sensitive to >440 keV protons [see *Evans and Greer*, 2000], a small flux enhancement due to the solar proton contamination can be found just after the shock arrival, particularly at L > 6.0. From an examination of the 240−800 keV ion measurement by the same NOAA satellites, we further confirmed that the proton contamination does not affect other results in this paper. In CME-associated storms, around the *Dst* minimum at t = 0.5 day, the flux enhancement takes place at L = 3.5. In CIR-associated storms, around the *Dst* minimum at t = 0.3 day, the flux enhancement takes place at L = 3.5−4.0. The radial expansion speed of the outer belt is faster and the generated flux during the recovery phase is much larger in CIR-associated storms than those of CME-associated storms.

[20] The criterion used at NOAA/SEC for the electron flux alert is >10^3 pfu of GOES >2.0 MeV flux. For a space weather application, the superposed epoch analysis in this study gives some clues about when and how often the electron flux exceeds the alert level after shock/stream interface arrivals. Figure 7 shows the occurrence probability of the electron flux alert using daily maximum flux. The occurrence probability 1 day after the shock is only 14% (7 of 49 events) and smaller than the prestorm level, while the probability 4 days after the shock increases to 43% (21 of 49 events) and larger than the prestorm level. In CIR-associated storms, it is 83% (5 of 6 events) 1 day after the interface arrival and remains at that level for at least 4 days. Note that the occurrence probabilities derived in this study are only applicable to the subset of events with *Dst* < −100 nT, and not to any shocks or stream interfaces.

[21] The occurrence probability is higher in CIR-associated storms even before the stream interface arrival because the solar cycle dependence of the background electron flux at geosynchronous orbit leads to a significantly

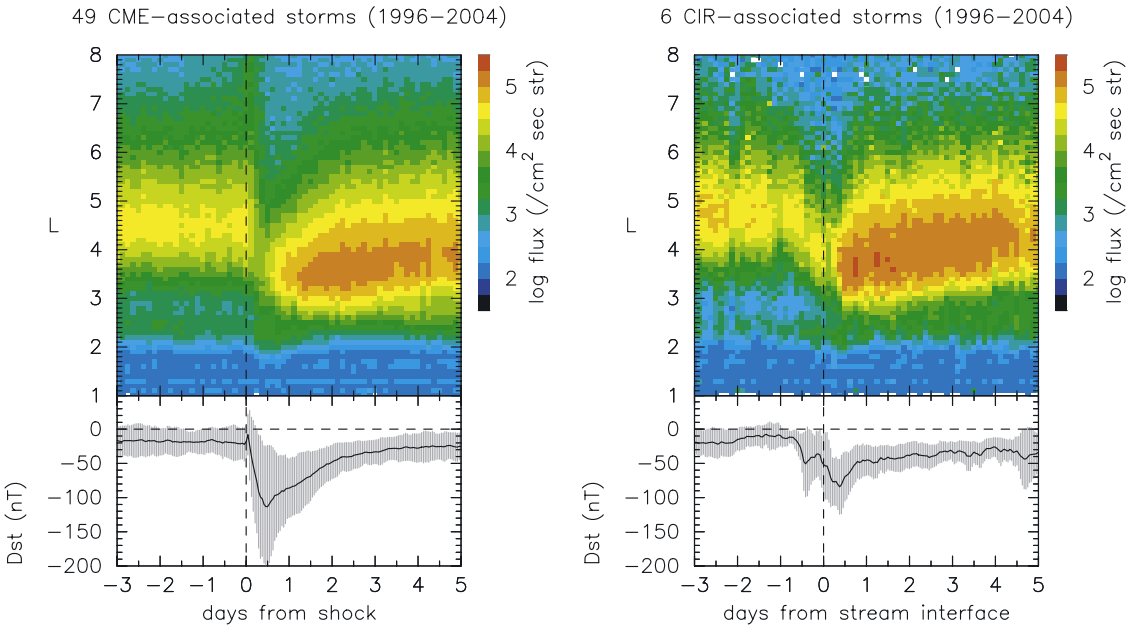

Figure 6. $L - t$ diagrams of >300 keV electrons measured by the NOAA/POES satellites, superposed about shocks and stream interfaces during (left) CME- and (right) CIR-associated storms, respectively. Averaged $\log_{10}$ flux is color coded from blue to red. Averaged *Dst* is also shown in the bottom plots. The gray region indicates the standard deviation.

higher flux in the declining phase of the solar cycle [*Miyoshi et al.*, 2004] where 4 of 6 CIR-associated storm events occurred. Table 4 shows the yearly averaged occurrence probabilities from 1996 to 2004. The averaged occurrence probabilities during the years of CIR-associated storms (1996, 1998, 2002, 2003, 2004) and CME-associated storms (1997–2004) are 45% and 34%, respectively, and are more consistent with the larger prestorm probabilities for CIR-associated storms (50%) than for CME-associated storms (25%).

5. Discussion

[22] Using a superposed epoch analysis centered on shocks and stream interfaces for CME- and CIR-associated storms, respectively, we quantitatively examined the average variations of the solar wind and magnetospheric parameters (Figures 3 and 4), the responses of radiation belt electrons (Figures 5 and 6), and the occurrence probability of the NOAA/SEC electron flux alert (Figure 7). These results themselves are important as a guideline to understand the relationship between the solar wind parameters and the solar wind structures, and useful for operational space weather forecasts by making probabilistic predictions of killer electrons.

[23] On average, CIR-associated storms are found to be more effective in producing flux enhancements at geosynchronous orbit than are CME-associated storms. This is consistent with the results obtained by *Dmitriev et al.* [2005] and *Miyoshi and Kataoka* [2005]. As the most important cause of this effectiveness of CIR-associated storms at geosynchronous orbit, we suggest the fluctuating electric field associated with the Alfvénic turbulence embedded in the high-speed coronal hole stream. *Tsurutani et al.* [2006] explained that such a solar wind structure usually causes a particular type of magnetospheric phenomenon called "High-Intensity Long-Duration Continuous AE Activities" (HILDCAAs), which is a suitable magnetospheric condition for the flux enhancement. Conversely, the reason why CME-associated storms cannot produce the flux enhancement as frequently as CIR-associated storms do is

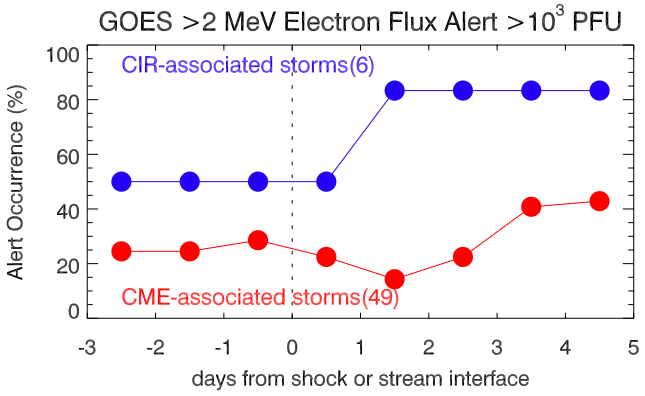

Figure 7. Occurrence probability of GOES >2.0 MeV electron flux alert with $>10^3$ pfu after shocks and stream interfaces for CME- (red) and CIR-associated storms (blue), respectively.

Table 4. Yearly Averaged Occurrence Probabilities of NOAA Alert Events With Daily Maximum Flux >1000 pfu[a]

Year	Days	Events	Alert, %
1996	366	96	26
1997	362	69	19
1998	363	103	28
1999	365	104	28
2000	362	83	23
2001	357	34	10
2002	364	67	18
2003	358	308	86
2004	366	240	66

[a]From left to right are shown the total number of available days of the GOES electron data, number of the NOAA alert events, and the occurrence probability of the NOAA alert.

that, during the recovery phase, such a strongly fluctuating magnetic field activity does not exist because of smooth magnetic field rotations inherent in magnetic clouds [*Burlaga et al.*, 1981].

[24] Large flux enhancements are frequently observed in the declining phase of the solar cycle [*Miyoshi et al.*, 2004]. The solar cycle dependence is also consistent with our hypothesis that the fluctuating electric field in the coronal hole stream is the most powerful energy source. Note also that, since the strength of CIR-driven storms is usually weak to moderate [*Tsurutani et al.*, 1995], many large flux events are associated with weaker storms with $Dst > -100$ nT. The results obtained in this paper for CIR-associated storms, however, can be naturally extended to the weaker CIR-related storms, considering the fact that our results are very similar as those of *McPherron et al.* [2005]. Superposing all of the CIR events in 1995 about the stream interfaces, *McPherron et al.* [2005] showed that the flux recovers to the prestorm level 1 day after the interface arrival, and enhances about one order of magnitude larger than the prestorm level in a few days.

[25] Here we discuss other possible effects originating from the solar wind parameter change, that lead to the different recovery phase in CIR-associated storms from that in CME-associated storms. During the recovery phase, Alfvén Mach number and magnetosonic Mach number are higher in the CIR-associated storms, which are more effective in producing a geoeffective magnetosheath [*Lopez et al.*, 2004; *Kataoka et al.*, 2005b]. Such a Mach number effect can modulate the energy source and may suppress the energy transfer during CME-associated storms. On the other hand, since plasma sheet temperatures are largely controlled by the solar wind speed, and plasma sheet densities are largely controlled by the solar wind density [*Borovsky et al.*, 1998; *Tsyganenko and Mukai*, 2003], the plasma sheet is expected to be hotter with lower densities during the recovery phase in CIR-associated storms. Such a difference in magnetospheric background properties may also be important in understanding the effective acceleration mechanism of energetic particles.

[26] The occurrence probabilities derived in this study are only applicable to the subset of events with $Dst < -100$ nT, and not to any shocks or stream interfaces. We are extending this study using all shocks and all stream interfaces observed during solar cycle 23 without using any criteria about *Dst* because such survey may be actually more general and can be practical for forecasting. On the basis of this study, we can update and modify our forecast when we see the strong enhancement of ring current. Real-time monitoring system of the evolution of a part of ring current has been successfully in operation in NICT Japan using low-latitude magnetometer at Okinawa, thus the results obtained in this paper are immediately useful for present space weather forecast service.

6. Conclusion

[27] Interplanetary shocks and stream interfaces are useful precursors for predicting flux enhancements during CME- and CIR-associated storms, respectively. On average, CIR-associated storms are more effective in the flux enhancement than are CME-associated storms, and the flux enhancement at geosynchronous orbit is roughly twice as fast and ten times stronger. In CME-associated storms, the average flux recovers to the prestorm level about 2 days after a shock arrival. The occurrence probability of the >2 MeV electron flux alert with $>10^3$ pfu at geosynchronous orbit 1 day after the shock is only 14% (7 of 49 events) and smaller than the prestorm level, while the probability 4 days after the shock increases to 43% (21 of 49 events) and is larger than the prestorm level. In CIR-associated storms, the average flux recovers to the prestorm level about 1 day after a stream interface arrival. The probability of an electron flux alert is 83% (5 of 6 events) 1 day after the stream interface arrival, and remains at that level for at least next 4 days. The occurrence probability of the killer electrons derived in this study offers a way to develop the advantages in probabilistic forecast for operational space weather forecasts.

[28] **Acknowledgments.** We would like to thank Jonathan Eastwood and Don Fairfield for their careful reading of the manuscript. The OMNI-2 data are provided from NASA/NSSDC. The NOAA/POES and GOES data are provided by NOAA/NGDC. R.K. acknowledges useful discussions at the LWS CDAW 2005 workshop. R.K. is supported by a research fellowship of the Japan Society for the Promotion of Science for Young Scientists.

References

Baker, D. N., J. B. Blake, R. W. Klebesadel, and P. R. Higbie (1986), Highly relativistic electrons in the Earth's outer magnetosphere: 1. Lifetimes and temporal history 1979–1984, *J. Geophys. Res.*, *91*, 4265–4276.

Baker, D. N., R. D. Belian, P. R. Higbie, R. W. Klebesadel, and J. B. Blake (1987), Deep dielectric charging effects due to high energy electrons in the Earth's outer magnetosphere, *J. Electrost.*, *20*, 3–19.

Baker, D. N., R. L. McPherron, T. E. Cayton, and R. W. Klebesadel (1990), Linear prediction filter analysis of relativistic electron properties at 6.6 R_E, *J. Geophys. Res.*, *95*, 15,133–15,140.

Baker, D. N., J. H. Allen, S. G. Kanekal, and G. D. Reeves (1998), Disturbed space environment may have been related to pager satellite failure, *Eos Trans. AGU*, *79*, 477.

Barker, A. B., X. Li, and R. S. Selesnick (2005), Modeling the radiation belt electrons with radial diffusion driven by the solar wind, *Space Weather*, *3*, S10003, doi:10.1029/2004SW000118.

Belcher, J. W., and L. Davis (1971), Large-amplitude Alfvén waves in the interplanetary medium, 2, *J. Geophys. Res.*, *76*, 3534–3563.

Blake, J. B., D. N. Baker, N. Turner, K. W. Ogilvie, and R. P. Lepping (1997), Correlation of changes in the outer-zone relativistic-electron population with upstream solar wind and magnetic field measurements, *Geophys. Res. Lett.*, *24*(8), 927–930.

Borovsky, J. E., and J. T. Steinberg (2006), The ''calm before the storm'' in CIR/magnetosphere interactions: Occurrence statistics, solar wind statistics, and magnetospheric preconditioning, *J. Geophys. Res.*, *111*, A07S10, doi:10.1029/2005JA011397.

Borovsky, J. E., M. F. Thomsen, and R. C. Elphic (1998), The driving of the plasma sheet by the solar wind, *J. Geophys. Res.*, *103*, 17,617–17,640.

Burlaga, L. F. (1974), Interplanetary stream interfaces (of solar wind), *J. Geophys. Res.*, *79*, 3717–3725.

Burlaga, L. F., E. Sittler, F. Mariani, and R. Schwenn (1981), Magnetic loop behind an interplanetary shock: Voyager, Helios and IMP-8 observations, *J. Geophys. Res.*, *86*, 6673–6684.

Burlaga, L. F., R. M. Skoug, C. W. Smith, D. F. Webb, T. H. Zurbuchen, and A. Reinard (2001), Fast ejecta during the ascending phase of solar cycle 23: ACE observations, 1998–1999, *J. Geophys. Res.*, *106*, 20,957–20,978.

Dmitriev, A. V., N. B. Crosby, and J.-K. Chao (2005), Interplanetary sources of space weather disturbances in 1997 to 2000, *Space Weather*, *3*, S03001, doi:10.1029/2004SW000104.

Evans, D. S., and M. S. Greer (2000), Polar orbiting environmental satellite space environment monitor: 2. Instrument description and archive data documentation, *NOAA Tech. Memo. OAR SEC-93*.

Friedel, R. H. W., G. D. Reeves, and T. Obara (2002), Relativistic electron dynamics in the inner magnetosphere---A review, *J. Atmos. Sol. Terr. Phys.*, *64*, 265–282.

Gonzalez, W. D., B. T. Tsurutani, and A. L. Gonzalez (1999), Interplanetary origin of geomagnetic storms, *Space Sci. Rev.*, *88*, 529–562.

Gosling, J. T., J. R. Asbridge, S. J. Bame, and W. C. Feldman (1978), Solar wind stream interfaces, *J. Geophys. Res.*, *83*, 1401–1412.

Huttunen, K. E. J., and H. E. J. Koskinen (2004), Importance of post-shock streams and sheath region as drivers of intense magnetospheric storms and high-latitude activity, *Ann. Geophys.*, *22*, 1729–1738.

Kataoka, R., S. Watari, N. Shimada, H. Shimazu, and K. Marubashi (2005a), Downstream structures of interplanetary fast shocks associated with coronal mass ejections, *Geophys. Res. Lett.*, *32*, L12103, doi:10.1029/2005GL022777.

Kataoka, R., D. H. Fairfield, D. G. Sibeck, L. Rastätter, M.-C. Fok, T. Nagatsuma, and Y. Ebihara (2005b), Magnetosheath variations during the storm main phase on 20 November 2003: Evidence for solar wind density control of energy transfer to the magnetosphere, *Geophys. Res. Lett.*, *32*, L21108, doi:10.1029/2005GL024495.

Li, X. (2004), Variations of 0.7–6.0 MeV electrons at geosynchronous orbit as a function of solar wind, *Space Weather*, *2*, S03006, doi:10.1029/2003SW000017.

Li, X., M. Temerin, D. N. Baker, G. D. Reeves, and D. Larson (2001), Quantitative prediction of radiation belt electrons at geostationary orbit based on solar wind measurements, *Geophys. Res. Lett.*, *28*(9), 1887–1890.

Li, X., D. N. Baker, M. Temerin, G. Reeves, R. Friedel, and C. Shen (2005), Energetic electrons, 50 keV to 6 MeV, at geosynchronous orbit: Their responses to solar wind variations, *Space Weather*, *3*, S04001, doi:10.1029/2004SW000105.

Lopez, R. (1987), Solar cycle invariance in solar wind proton temperature relationships, *J. Geophys. Res.*, *92*, 11,189–11,194.

Lopez, R. E., M. Wiltberger, S. Hernandez, and J. G. Lyon (2004), Solar wind density control of energy transfer to the magnetosphere, *Geophys. Res. Lett.*, *31*, L08804, doi:10.1029/2003GL018780.

McPherron, R. L., and G. Siscoe (2004), Probabilistic forecasting of geomagnetic indices using solar wind air mass analysis, *Space Weather*, *2*, S01001, doi:10.1029/2003SW000003.

McPherron, R. L., G. Siscoe, N. Crooker, and N. Arge (2005), Probabilistic forecasting of the *Dst* index, in *The Inner Magnetosphere: Physics and Modeling*, *Geophys. Monogr. Ser.*, vol. *155*, edited by T. I. Pulkkinen, N. A. Tsyganenko, and R. H. W. Friedel, pp. 203–210, AGU, Washington, D. C.

Miyoshi, Y., and R. Kataoka (2005), Ring current ions and radiation belt electrons during geomagnetic storms driven by coronal mass ejections and corotating interaction regions, *Geophys. Res. Lett.*, *32*, L21105, doi:10.1029/2005GL024590.

Miyoshi, Y., A. Morioka, H. Misawa, T. Obara, T. Nagai, and Y. Kasahara (2003), Rebuilding process of the outer radiation belt during the 3 November 1993 magnetic storm: NOAA and Exos-D observations, *J. Geophys. Res.*, *108*(A1), 1004, doi:10.1029/2001JA007542.

Miyoshi, Y. S., V. K. Jordanova, A. Morioka, and D. S. Evans (2004), Solar cycle variations of the electron radiation belts: Observations and radial diffusion simulation, *Space Weather*, *2*, S10S02, doi:10.1029/2004SW000070.

Nihon Keizai Shimbun (2004), BS digital broadcasting temporarily stopped (in Japanese), 15 Feb.

Ober, D. M., N. C. Maynard, and W. J. Burke (2003), Testing the Hill model of transpolar potential saturation, *J. Geophys. Res.*, *108*(A12), 1467, doi:10.1029/2003JA010154.

Paulikas, G. A., and J. B. Blake (1979), Effects of the solar wind on magnetospheric dynamics: Energetic electrons at the synchronous orbit, in *Quantitative Modeling of Magnetospheric Processes*, *Geophys. Monogr. Ser.*, vol. *21*, edited by W. P. Olsen, pp. 180–202, AGU, Washington, D. C.

Reeves, G. D., K. L. McAdams, R. H. W. Friedel, and T. P. O'Brien (2003), Acceleration and loss of relativistic electrons during geomagnetic storms, *Geophys. Res. Lett.*, *30*(10), 1529, doi:10.1029/2002GL016513.

Richardson, I. G., and H. V. Cane (1995), Regions of abnormally low proton temperature in the solar wind (1965–1991) and their association with ejecta, *J. Geophys. Res.*, *100*, 23,397–23,412.

Richardson, I. G., et al. (2006), Major geomagnetic storms ($Dst \leq -100$ nT) generated by corotating interaction regions, *J. Geophys. Res.*, *111*, A07S09, doi:10.1029/2005JA011476.

Shue, J.-H., et al. (1998), Magnetopause location under extreme solar wind conditions, *J. Geophys. Res.*, *103*, 17,691–17,700.

Siscoe, G. L., G. M. Erickson, B. U. Ö. Sonnerup, N. C. Maynard, J. A. Schoendorf, K. D. Siebert, D. R. Weimer, W. W. White, and G. R. Wilson (2002), Hill model of transpolar potential saturation: Comparisons with MHD simulations, *J. Geophys. Res.*, *107*(A6), 1075, doi:10.1029/2001JA000109.

Smith, E. J. (2001), The heliospheric current sheet, *J. Geophys. Res.*, *106*, 15,819–15,831.

Tsurutani, B. T., W. D. Gonzalez, A. L. C. Gonzalez, F. Tang, J. K. Arballo, and M. Okada (1995), Interplanetary origin of geomagnetic activity in the declining phase of the solar cycle, *J. Geophys. Res.*, *100*, 21,717–21,734.

Tsurutani, B. T., et al. (2006), Corotating solar wind streams and recurrent geomagnetic activity: A review, *J. Geophys. Res.*, *111*, A07S01, doi:10.1029/2005JA011273.

Tsyganenko, N. A., and T. Mukai (2003), Tail plasma sheet models derived from Geotail particle data, *J. Geophys. Res.*, *108*(A3), 1136, doi:10.1029/2002JA009707.

Yoshida, A., T. Toya, and M. Yoshida (2004), Solar-cycle and semi-annual variations of magnetic storms, *J. Geogr.*, *113*(1), 107–124.

R. Kataoka and Y. Miyoshi, Solar-Terrestrial Environment Laboratory, Nagoya University, Furo-cho, Chikusa-ku, Nagoya, Aichi 464-8601, Japan. (ryuho@stelab.nagoya-u.ac.jp)